

## Identification of Cavities in a Three-Dimensional Layer by Minimization of an Optimal Cost Functional Expansion

A.E. Martínez-Castro <sup>1</sup>, I.H. Faris <sup>1</sup>, and R. Gallego <sup>1</sup>

**Abstract:** In this paper, the identification of hidden defects inside a three-dimensional layer is set as an Identification Inverse Problem. This problem is solved by minimizing a cost functional which is linearized with respect to the volume defects, leading to a procedure that requires only computations at the host domain free of defects. The cost functional is stated as the misfit between experimental and computed displacements and spherical and/or ellipsoidal cavities are the defects to locate. The identification of these cavities is based on the measured displacements at a set of points due to time-harmonic point loads at an array of source points. The topological expansion of the displacement field due to the presence of a small cavity provides the topological expansion of the cost functional. This expansion, called the Cost Functional Expansion, depends quadratically on the cavity volumes. Therefore, considering that the cavity center coordinates are fixed, the optimum volumes of the defects are easily computed by a closed-form formula. The evaluation of the Cost Functional Expansion for the optimum cavity volumes defines the Optimal Cost Functional Expansion, which depends only on the cavity center coordinates. The evaluation of the Optimal Cost Functional Expansion is very fast since it depends only on information computed at the non-damaged layer. Finally, a zero-order algorithm, such as Genetic Algorithms is proposed to find the optimal positions of the cavity centers. A set of numerical tests have been carried out, in order to test the main properties of the proposed procedure. It is shown to be a very effective technique to find hidden cavities in problems in which no a-priori information is known with respect to the number, position and size of defects.

**Keywords:** Topological Derivative, Identification Inverse Problems, Genetic Algorithms, Experimental Noise, Layered media, Elastodynamics, Boundary Elements

---

<sup>1</sup> University of Granada, Granada, Spain

## 1 Introduction

The identification of cavities embedded in an elastic solid is a long-standing problem in inverse analysis. The so called Identification Inverse Problem (IIP) can be solved as an optimization problem, in which a cost functional is built based on the difference between the results obtained by some experimental procedure, and those obtained from a model. The algorithm requires the computation of a forward problem at each iteration, with an explicit or semi-analytic computation of gradients (adjoint variable approach). The forward solution is usually computed by a numerical technique, such as the Boundary Element Method (BEM), which permits the fast evaluation of different solutions when shape variations are prescribed in some part of the domain.

An alternative approach to solve the forward problem is the use of a small-cavity expansion. With this approach, the displacement and traction fields at the damaged domain are approximated from the direct values and volume derivatives computed at the non-damaged domain. This alternative approach requires the computation of the so-called Topological Sensitivity (TS), or Topological Derivative (TD). Once the topological expansion is carried out for displacements and/or tractions, such expansion can be used to expand the cost functional of the IIP. The main advantages of this approach are: i) the fast computation of the forward problem; ii) the possibility of obtaining zero volumes as optimal parameters (the trial cavity is removed from the search space).

The first papers in which the TD is used in the context of optimization problems was presented in [Eschenauer, Kobelev, and Schumacher (1994)] and [Schumacher (1995)]. The generalization to shape inverse problems was carried out by Sokołowski and co-workers [Sokołowski and Żochowski (1997, 1998); Lewiński and Sokołowski (1997, 1998); Jackowska-Strumiłło, Sokołowski, and Żochowski (1999); Lewiński and Sokołowski (2003)].

A Boundary Integral Equation (BIE) for the computation of the TD was developed by Gallego and Rus [Gallego and Rus (2002, 2004)]. In such work, the TD-BIE of displacements and tractions is derived in a closed-form formula for two-dimensional elasticity problems both for circular cavities and cracks. The topological expansion of displacements and tractions leads to the definition of an approximated cost functional, which permit the statement of a global optimization algorithm to find a minimum. This approximated cost functional can be minimized with global search techniques, such as the Genetic Algorithm (GA) approach. The technique is extended to the analysis of anisotropic solids in two-dimensional elastostatic problems [Comino, Gallego, and Rus (2008)].

The use of the TD as an image method to find initial shapes of hidden objects for

three-dimensional elasticity problems in the context of BIEs is proposed by Guzina and Bonnet [Guzina and Bonnet (2004); Bonnet and Guzina (2004); Guzina and Chikichev (2007)].

In the present work, the linearized topological expansion of the cost functional is used, combined with GA to find the optimal positions and volumes of the spherical hidden cavities. The host domain is a three-dimensional viscoelastic layer. The forward problem is solved by using the Green function of a single-layered domain [Martínez-Castro and Gallego (2007)], and therefore the upper and lower free stress surfaces are not meshed. Pseudo-experimental data are generated by solving a forward problem by BEM. The formulation is also extended to the case of multiple defect identification, neglecting the interaction between cavities and cavity-free surface. A numerical benchmark is carried out in order to observe the dependence of the minimization process on different parameters such as experimental noise and material damping.

## 2 Forward Problem

A three-dimensional viscoelastic layer, with a set of dynamic harmonic sources and a hidden spherical cavity is the basic problem considered. In reference to Fig. 1, the host domain is the three-dimensional layer  $\Omega$ , thickness  $h$ . In reference to the Cartesian basis  $\mathcal{B}\{O; x_1, x_2, x_3\}$ , the domain is given by the set  $\Omega = \{(x_1, x_2, x_3) \mid 0 \leq x_3 \leq h\}$ , bounded by two traction-free planes  $\Gamma = \{(x_1, x_2, x_3) \mid x_3 = 0\} \cup \{(x_1, x_2, x_3) \mid x_3 = h\}$ .

The hidden cavity is a sphere  $\Omega_z$ , bounded by  $\Gamma_z$ , centered at  $\mathbf{z}$  and has radius  $a_r$ . In Fig. 1 the outward cavity normal  $\mathbf{n}$  is represented, pointing towards the cavity center.

Let consider a set of points  $\mathbf{x}_n^s$  on the upper surface where point load time-harmonic sources are applied. Hence, the loads are given by,

$$\mathbf{f}(\mathbf{x}) = \sum_{n=1}^{NS} P_n e^{i\omega t} \delta(\mathbf{x} - \mathbf{x}_n^s) \mathbf{e}_3 \quad (1)$$

where  $\delta$  stands for the three-dimensional Dirac delta function;  $P_n$  are the force magnitudes and  $\mathbf{e}_3$  the unit vector in the  $x_3$  direction. With this reference, the forward problem is stated as,

$$\begin{aligned} \nabla \cdot (\mathbf{C} : \nabla \mathbf{u}) + \mathbf{f} + \rho \omega^2 \mathbf{u} &= \mathbf{0}, & \mathbf{x} \in \Omega \setminus \Omega_z \\ \mathbf{t} &= \mathbf{0}, & \mathbf{y} \in \Gamma \cup \Gamma_z \end{aligned} \quad (2)$$

where  $\mathbf{t}$  is the traction vector, and  $\mathbf{C}$  is the elastic tensor, that in this case is considered isotropic. Additionally, the solution should fulfill the radiation condition

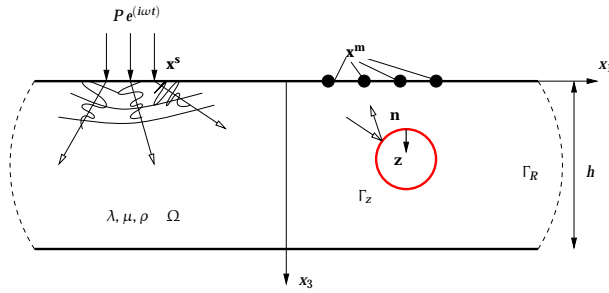


Figure 1: Spherical cavity in a single layer domain. Sources and measurement points

at infinity. The time-harmonic response includes damping, through the damping rates  $\xi_\alpha$  y  $\xi_\beta$  and the complex-valued material modules  $\mu^* = \mu(1 + 2i\xi_\alpha(\omega))$  and  $\lambda^* + 2\mu^* = (\lambda + 2\mu)(1 + 2i\xi_\beta(\omega))$ , by virtue of the *corresponding principle* [Christensen (1971)].

For a point  $\mathbf{x} \in \Omega \setminus \Omega_z$ , the basic elastodynamic BIE can be stated as,

$$u_i(\mathbf{x}) + \int_{\Gamma_z} \hat{t}_k^i(\mathbf{y}; \mathbf{x}) u_k(\mathbf{y}) d\Gamma(\mathbf{y}) = \sum_{n=1}^{NS} P_n \hat{u}_3^i(\mathbf{x}_n^s; \mathbf{x}) \quad (3)$$

where  $\hat{u}_k^i(\mathbf{y}; \mathbf{x})$  and  $\hat{t}_k^i(\mathbf{y}; \mathbf{x})$  are the displacement and traction functions of the fundamental solution for the layer [Martínez-Castro and Gallego (2007)]. Note that this fundamental solution fulfills the traction free boundary conditions at both the upper and lower surfaces, and therefore only the integration along the cavity surface appears in the BIE.

The previous equation, when stated at the Non-Damaged State (NDS), i.e., the layer domain  $\Omega$  without any cavity, consists on the direct collocation of the Fundamental Solution, since the BIE simplifies to,

$$u_i(\mathbf{x}) = \sum_{n=1}^{NS} P_n \hat{u}_3^i(\mathbf{x}_n^s; \mathbf{x}) \quad (4)$$

### 3 Inverse Problem

The Inverse Identification Problem (IIP) is stated as the location of the hidden cavity  $\Omega_z$  (or cavities as it will shown in the following sections). Displacements  $\tilde{\mathbf{u}}^m = \tilde{\mathbf{u}}(\mathbf{x}^m)$  are computed at points  $\mathbf{x}^m \in \Gamma$  (see Fig. 1) for an assumed cavity. On the other hand, the experimental values of the displacement,  $\mathbf{u}^{e,m}$  are those obtained

for the true position and size of the cavity, at the same points  $\mathbf{x}^m$ . In the context of this work, such displacements are not obtained by a real experiment but computed numerically by a BEM model.

The cost functional is defined by,

$$\mathcal{J}(\Gamma) = \sum_{m=1}^{\text{NEP}} \frac{1}{2} (\overline{\mathbf{u}^m - \mathbf{u}^{e,m}})^T (\mathbf{u}^m - \mathbf{u}^{e,m}) \quad (5)$$

where NEP is the number of experimental points. The overlined term represents the conjugate complex of the displacement difference.

#### 4 Topological Derivative Boundary Integral Equation

The approach to obtain the TD elastodynamic BIE is similar to the one carried out in [Gallego and Rus (2002)] for static problems. The displacement  $\mathbf{u}$  at an internal point  $\mathbf{x} \in \Omega$  when there is no defect is computed by evaluating the Green function, as shown in Eq. 4. The presence of a traction-free small cavity bounded by  $\Gamma_z$  located at  $\mathbf{z}$  produces the modified displacement field  $\tilde{\mathbf{u}}$ . This second state is called the *Damaged State* (DS). The BIE for the displacement field  $\tilde{\mathbf{u}}$  at  $\mathbf{x}$  is,

$$\tilde{u}_i(\mathbf{x}) + \int_{\Gamma_z} \hat{t}_k^i(\mathbf{y}; \mathbf{x}) \tilde{u}_k(\mathbf{y}) d\Gamma(\mathbf{y}) = \sum_{n=1}^{NS} P_n \hat{u}_3^i(\mathbf{x}_n^s; \mathbf{x}) \quad (6)$$

Now, the displacement field at the cavity boundary  $\Gamma_z$  can be split as  $\tilde{u}_k(\mathbf{y}) = u_k^0(\mathbf{z}) + \Delta \tilde{u}_k(\mathbf{z})$ , where  $u_k^0(\mathbf{z})$  is a rigid-body displacement, and  $\Delta \tilde{u}_k(\mathbf{y})$  is the displacement field relative to the center  $\mathbf{z}$  due to the local state of stresses.

Therefore, the integral in Eq. 6 can be split into two terms, by virtue of the displacement field decomposition,

$$\int_{\Gamma_z} \hat{t}_k^i(\mathbf{y}; \mathbf{x}) \tilde{u}_k(\mathbf{y}) d\Gamma(\mathbf{y}) = u_k^0(\mathbf{z}) \int_{\Gamma_z} \hat{t}_k^i(\mathbf{y}; \mathbf{x}) d\Gamma(\mathbf{y}) + \int_{\Gamma_z} \hat{t}_k^i(\mathbf{y}; \mathbf{x}) \Delta \tilde{u}_k(\mathbf{y}) d\Gamma(\mathbf{y}) \quad (7)$$

The first integral in Eq. 7 right-hand side is transformed by the divergence theorem,

$$\int_{\Gamma_z} \hat{t}_k^i(\mathbf{y}; \mathbf{x}) d\Gamma(\mathbf{y}) = - \int_{\Omega_z} \hat{\sigma}_{k,j}^i(\mathbf{z}; \mathbf{x}) d\Omega = \mathcal{V}(\mathbf{z}) \rho \omega^2 \hat{u}_k^i(\mathbf{z}; \mathbf{x}) \quad (8)$$

where  $\mathcal{V}(\mathbf{z}) = 4/3 \pi r^3$  is the spherical cavity volume at  $\mathbf{z}$ . Taking into account that for a vanishing cavity,  $u_k^0(\mathbf{z}) = u_k(\mathbf{z}) + \text{h.o.t.}$  where h.o.t. stands for *higher order terms*, and  $u_k(\mathbf{z})$  is the displacement at point  $\mathbf{z}$  in the NDS. Therefore, the first term in Eq. 7 right-hand side is written as,

$$u_k^0(\mathbf{z}) \int_{\Gamma_z} \hat{t}_k^i(\mathbf{y}; \mathbf{x}) d\Gamma(\mathbf{y}) = \mathcal{V}(\mathbf{z}) \rho \omega^2 \hat{u}_k^i(\mathbf{z}; \mathbf{x}) u_k(\mathbf{z}) \quad (9)$$

The second integral at the right-hand side in Eq. 7 includes a displacement field  $\Delta\bar{u}_k(\mathbf{y})$ . To first order, the stresses at any point inside the domain  $\mathbf{x}$  far from the flaw location are equal to those of the NDS,  $\hat{\sigma}_{ij}(\mathbf{x}) = \sigma_{ij}(\mathbf{x}) + \text{h.o.t.}$ . Furthermore, the stresses at  $\mathbf{x}$  around the cavity in the NDS are, to first order,  $\sigma_{ij}(\mathbf{x}) = \sigma_{ij}(\mathbf{z}) + \text{h.o.t.}$ . Therefore, when the size of the cavity goes to zero, it is subject to a stress field that is like the one of the NDS state at the cavity center. Thus, the displacements  $\Delta\bar{u}_k(\mathbf{y})$  along the vanishing flaw are,

$$\Delta\bar{u}_k(\mathbf{y}) = \Delta u_k^\infty(\mathbf{y}) + \text{h.o.t.} \tag{10}$$

where  $\Delta u_k^\infty(\mathbf{y})$  represents the displacements due to a remote stress field  $\sigma_{ij}(\mathbf{z})$  in an infinite domain.

On the other hand, with regards to the traction  $\hat{t}_k^i(\mathbf{y}; \mathbf{x})$ , to first order,

$$\hat{t}_k^i(\mathbf{y}; \mathbf{x}) = \hat{\sigma}_{jk}^i(\mathbf{y}; \mathbf{x})n_j(\mathbf{y}) = \hat{\sigma}_{jk}^i(\mathbf{z}; \mathbf{x})n_j(\mathbf{y}) + \text{h.o.t.} \tag{11}$$

Therefore, the second integral term at the right-hand side in Eq. 7 is evaluated as:

$$\int_{\Gamma_z} \hat{t}_k^i(\mathbf{y}; \mathbf{x})\Delta\bar{u}_k(\mathbf{y})d\Gamma(\mathbf{y}) = \hat{\sigma}_{jk}^i(\mathbf{z}; \mathbf{x}) \int_{\Gamma_z} n_j(\mathbf{y})\Delta u_k^\infty(\mathbf{y})d\Gamma(\mathbf{y}) + \text{h.o.t.} \tag{12}$$

Finally, Eq. 6 can be written as,

$$\begin{aligned} \tilde{u}_i(\mathbf{x}) &+ \mathcal{V}(\mathbf{z})\rho\omega^2\hat{u}_k^i(\mathbf{z}; \mathbf{x})u_k(\mathbf{z}) \\ &+ \hat{\sigma}_{jk}^i(\mathbf{z}; \mathbf{x}) \int_{\Gamma_z} n_j(\mathbf{y})\Delta u_k^\infty(\mathbf{y})d\Gamma(\mathbf{y}) + \text{h.o.t.} = \sum_{n=1}^{NS} P_n\hat{u}_3^i(\mathbf{x}_n^S; \mathbf{x}) \end{aligned} \tag{13}$$

Subtracting to this BIE for the DS, Eq. 13, the corresponding one for the NDS, Eq. 3, one obtains,

$$\Delta u_i(\mathbf{x}) + \mathcal{V}(\mathbf{z})\rho\omega^2\hat{u}_k^i(\mathbf{z}; \mathbf{x})u_k(\mathbf{z}) + \hat{\sigma}_{jk}^i(\mathbf{z}; \mathbf{x}) \int_{\Gamma_z} n_j(\mathbf{y})\Delta u_k^\infty(\mathbf{y})d\Gamma(\mathbf{y}) + \text{h.o.t.} = 0 \tag{14}$$

Now, dividing by the cavity volume, taking the limit when the cavity volume goes to zero, the so-called TD-BIE is obtained [Gallego and Rus (2004)], in which the displacement TD,

$$\delta u_i(\mathbf{x}) = \lim_{\mathcal{V}(\mathbf{z}) \rightarrow 0} \frac{\Delta u_i(\mathbf{x})}{\mathcal{V}(\mathbf{z})} \tag{15}$$

is evaluated with the following BIE,

$$\delta u_i(\mathbf{x}) = -\rho\omega^2\hat{u}_k^i(\mathbf{z}; \mathbf{x})u_k(\mathbf{z}) - \hat{\sigma}_{jk}^i(\mathbf{z}; \mathbf{x}) \lim_{\mathcal{V}(\mathbf{z}) \rightarrow 0} \frac{1}{\mathcal{V}(\mathbf{z})} \int_{\Gamma_z} n_j(\mathbf{y})\delta u_k^\infty(\mathbf{y})d\Gamma(\mathbf{y}) \tag{16}$$

In Eq. 16 the last integral can be evaluated in a closed-form tensor [Eshelby (1957, 1959)], and it is easily shown that,

$$\int_{\Gamma_z} n_j(\mathbf{y}) \delta u_k^\infty(\mathbf{y}) d\Gamma(\mathbf{y}) = \mathcal{V}(\mathbf{z}) I_{jk}(\mathbf{z}) \quad (17)$$

where  $I_{jk}(\mathbf{z})$  is given by,

$$I_{jk}(\mathbf{z}) = -\frac{15(1-\nu)}{4(7-5\nu)\mu} \left[ 2\sigma_{jk}(\mathbf{z}) - \frac{1+5\nu}{5(1+\nu)} \delta_{jk} \sigma_{ii}(\mathbf{z}) \right] \quad (18)$$

thus, the TD-BIE for a spherical cavity is:

$$\delta u_i(\mathbf{x}) = -\rho \omega^2 \hat{u}_k^i(\mathbf{z}; \mathbf{x}) u_k(\mathbf{z}) - \hat{\sigma}_{jk}^i(\mathbf{z}; \mathbf{x}) I_{jk}(\mathbf{z}) \quad (19)$$

Bear in mind that no integral appears in this equation, and therefore the computation of  $\delta u_k(\mathbf{x})$  is a very low cost straightforward computation.

## 5 Topological expansion of the Cost Functional

The displacement field at any point  $\mathbf{x}$  can be linearized as follows,

$$\tilde{u}_k(\mathbf{x}) \simeq u_k(\mathbf{x}) + \mathcal{V}(\mathbf{z}) \delta u_k(\mathbf{x}) \quad (20)$$

where  $u_k(\mathbf{x})$  are the NDS displacements computed by Eq. 4, and  $\delta u_k(\mathbf{x})$  the TD of this field computed by Eq. 19. Again, it is worth remarking that these computations are inexpensive, since no integration is involved.

From the displacement linearization, the cost functional expansion can be computed as,

$$\mathcal{J}(\Gamma) \simeq \mathcal{J}^0 + \mathcal{V}(\mathbf{z}) \mathcal{T}(\mathbf{z}) + \mathcal{V}^2(\mathbf{z}) \mathcal{H}(\mathbf{z}) \quad (21)$$

with

$$\begin{aligned} \mathcal{J}^0 &= \sum_{m=1}^{NEP} \frac{1}{2} [\mathbf{u}^m - \mathbf{u}^{e,m}]^T [\mathbf{u}^m - \mathbf{u}^{e,m}] \\ \mathcal{T}(\mathbf{z}) &= \sum_{m=1}^{NEP} [\mathbf{u}^m - \mathbf{u}^{e,m}]^T \delta \mathbf{u}^m \\ \mathcal{H}(\mathbf{z}) &= \sum_{m=1}^{NEP} \frac{1}{2} [\delta \mathbf{u}^m]^T \delta \mathbf{u}^m \end{aligned} \quad (22)$$

The approximated cost functional represented by Eq. 21 is evaluated by easy computations at the NDS. For a given location of the cavity center  $\mathbf{z}$ , the cost functional

is evaluated in terms of the cavity volume  $\mathcal{V}(\mathbf{z})$  and the displacements at the measurement points  $\mathbf{x}^m$ ,  $\mathbf{u}^m$ , and their TD,  $\delta\mathbf{u}^m$ . Hence, given  $\mathbf{z}$ , a search of the optimum cavity volume  $\mathcal{V}^{\text{opt}}(\mathbf{z})$  that minimizes the expansion is possible. A constrained minimization is stated, with the restriction  $\mathcal{V}(\mathbf{z}) \geq 0$ .

The quadratic expansion of the cost functional represented by Eq. 21 is incomplete respect to its formal expansion based on the first and second order derivatives respect to the cavity volume. It is based on the linearization of the displacement field, but the second derivative of the cost functional with respect to the cavity volume would include second-order derivatives of displacements. This approach has been carried out in the literature [Bonnet (2009)]. Although a fully-quadratic expansion of displacement would improve the approximation of the cost functional, this kind of approach entails disadvantages in the context of the present work:

- More computing time for each cavity configuration. A basic requirement for the cost functional that permits the use of zero-order optimization algorithms, like GA, is the fast evaluation at each iteration. The aim of the present work is testing the more simple expansion, centering the analysis in the inverse problem uncertainties (damping, error in estimation points), and properties inherent to the global search.
- Numerical tests confirm that the expansion of the cost functional based on linearized displacements is practical, in the context of the 3D layer domain, which includes radiation damping.
- For dynamic problems in the frequency domain, the cost functional is also sensitive to the wavenumber; thus, the kind of quadratic expansion proposed represents the simplest and fastest way to obtain a forward solution at each trial configuration.
- This kind of second-order expansion is common in the context of optimization problem, in which an approximation to the Hessian matrix is employed without compromising the convergence (quasi-Newton methods).

### ***5.1 Topological Expansion for multiple cavity identification***

The topological expansion for the problem with  $n$  cavities requires the analysis of a new problem, in which a new sphere is generated in a domain with  $(n - 1)$  existing defects. The integral equation that defines the displacement derivative would include additional terms to consider the effects of the  $(n - 1)$  cavities into the new generated one.

At the present analysis, the interaction between cavities is neglected. Numerical examples confirm that the layer domain contains a radiation damping that permits

for some problems neglecting such effect, when each cavity is far enough from the surrounding cavities.

Let  $\mathbf{v}$  be a column vector whose  $v_j$  component represents the volume of the  $j$ -th cavity located at  $\mathbf{z}_j$ , i.e.,  $v_j = \mathcal{V}(\mathbf{z}_j)$ , where  $j = 1 \dots \text{NCAV}$  with NCAV, the total number of cavities. Let  $\mathbf{T}^m$  be a  $\text{MC} \times \text{NCAV}$ -matrix containing the TD of displacements at point  $\mathbf{x}^m$  with respect to a cavity located at  $\mathbf{z}_j$ , where MC are the number of measured components. Symbolically,

$$T_{ij} = \frac{\partial u_i(\mathbf{x}^m)}{\partial \mathcal{V}(\mathbf{z}_j)} \quad j = 1 \dots \text{NCAV} \quad (23)$$

where  $i$  are the measured components of displacement. Thus, the topological expansion of the displacement vector at a particular measurement point  $\mathbf{x}^m$  is written as,

$$\tilde{\mathbf{u}}^m = \mathbf{u}^m + \mathbf{T}^m \mathbf{v} \quad (24)$$

and therefore the topological expansion of the cost functional is obtained as follows,

$$\mathcal{J}(\Gamma) \simeq \mathcal{J}^0 + \mathbf{T}\mathbf{v} + \frac{1}{2}\mathbf{v}^T \mathbf{H}\mathbf{v} \quad (25)$$

where

$$\begin{aligned} \mathcal{J}^0 &= \sum_{m=1}^{NEP} \frac{1}{2} [\overline{\mathbf{u}^m - \mathbf{u}^{e,m}}]^T [\mathbf{u}^m - \mathbf{u}^{e,m}] \\ \mathbf{T} &= \sum_{m=1}^{NEP} \left( [\overline{\mathbf{u}^m - \mathbf{u}^{e,m}}]^T \mathbf{T}^m \right) \\ \mathbf{H} &= \sum_{m=1}^{NEP} \left( \overline{\mathbf{T}^m}^T \mathbf{T}^m \right) \end{aligned} \quad (26)$$

## 6 Optimal Cost Functional Expansion

The Optimal Cost Functional Expansion (OCFE) is defined as the value of the cost functional evaluated at the optimum volumes. In the context of multiple-cavity identification, Eq. 25 is minimized for a set of cavities at given positions. The optimum volume vector is computed by a simple constrained minimization, which can be summarized as follows.

- 1) Compute the optimum volume vector  $\mathbf{v}^{\text{opt}}$  by minimizing the cost functional in Eq. 25 finding the root of its first order derivative. A local equation system is stated,

$$\sum_{m=1}^{NEP} \left[ \overline{\mathbf{T}^m}^T \mathbf{T}^m \right] \mathbf{v}^{\text{opt}} = - \sum_{m=1}^{NEP} [\overline{\mathbf{u}^m - \mathbf{u}^{e,m}}]^T \mathbf{T}^m \quad (27)$$

- 2) If any component  $v_j^{\text{opt}} = \mathcal{V}(\mathbf{z}_j)^{\text{opt}}$  is negative, obtain the minimum of  $\mathbf{v}$  at the feasible region boundaries, i.e., at  $v_k = 0$ , with  $k = 1 \dots \text{NCAV}$ .
- 3) Select among the candidate optimum volume vectors found at previous step this which minimize the expansion in Eq. 25.

Once vector  $\mathbf{v}^{\text{opt}}$  is obtained, the OCFE is evaluated by the expression,

$$\mathcal{J}^{\text{opt}}(\Gamma) = \mathcal{J}^0 + \mathbf{T}\mathbf{v}^{\text{opt}} + \frac{1}{2} [\mathbf{v}^{\text{opt}}]^T \mathbf{H}\mathbf{v}^{\text{opt}} \quad (28)$$

The above equation provides the OCFE for a given set of cavities, and will provide an approximation of the optimal value of the full functional, but only involves computations in the NDS. The single cavity identification is a particularization of Eq. 28.

## 7 Numerical benchmark

At this section a numerical benchmark has been carried out in order to illustrate the applications of TD expansion in detection problems. The use of zero-order algorithms is convenient when the evaluation of the cost functional is inexpensive, in terms of computing effort, and when gradients of the cost functional with respect to the design parameters are difficult to obtain. Such is the case of the approximated cost functional proposed. Among the different zero-order algorithms reported in the literature to solve the IIP, Genetic Algorithms (GA) provides a fast and accurate solutions. The combined use of TD-GA is reported in the literature [Gallego and Rus (2002, 2004)].

In all cases a layer of thickness  $h = 6r$  is considered. Material parameters will be  $\mu$ ,  $\nu = 0.3$  and density  $\rho$ . Non-dimensional values of frequencies will be considered  $\bar{\omega} = \frac{\omega}{\omega^{\text{ref}}} = \{1.0, 1.5, 2.0, 2.5\}$  where  $\omega^{\text{ref}} = \frac{c_s}{r}$  with  $c_s = \sqrt{\frac{\mu}{\rho}}$  the S-wave speed. Therefore, the S-wave length  $\lambda_s = \frac{2\pi c_s}{\omega} = \frac{2\pi r}{\bar{\omega}}$  will take values  $\lambda_s = \{6.28r, 4.19r, 3.14r, 2.51r\}$ .

### 7.1 Single cavity detection

A single spherical cavity, radius  $a_r = 0.5r$  centered at  $(0, 0, 3r)$  is considered in this section. For this configuration, a set of experiments have been designed to analyze the dependence on certain parameters: sources/receivers profile, noise and material damping.

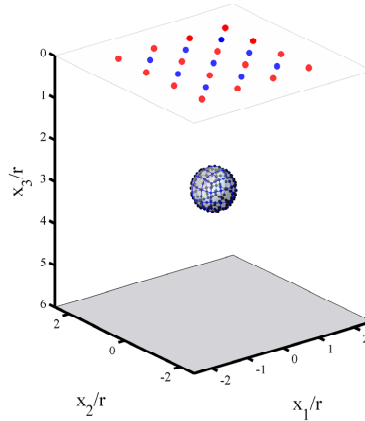


Figure 2: Configuration of sources (red) and receivers (blue). Identification of a centered cavity

### 7.1.1 Symmetric profile sources/receivers

For this set of tests, a symmetric profile of sources/receivers has been chosen. Both sources and receivers are centered at  $(0,0,0)$ . The sources array consists on 16 points disposed in a square patch of size  $4r \times 4r$ ; the receivers array consists on 9 points, disposed in a square patch of size  $3r \times 3r$ . In Fig. 2 the basic configuration of arrays of sources, receivers, layer, and true cavity position are shown. The figure also show the Boundary Element mesh used to compute the pseudo-experimental measurements. The sphere is meshed with 54 8-node quadratic elements. The number of nodes is 164.

### 7.1.2 Cost functional expansion

In this section the full functional versus the Cost Functional Expansion is computed for a simple problem, in order to show the validity and limitations of this expansion. The cost functional expansion is obtained for the single cavity identification. The cavity center is fixed at  $(0,0,3r)$  and the functionals are computed for different values of the cavity volume. In Fig. 3 the exact and the approximated cost functional are shown, in terms of the cavity volume, at two different frequencies  $\bar{\omega} = \{1.0, 2.0\}$ . The true radius value is  $a_r = 0.5r$ , with volume  $\mathcal{V} = 0.5236r^3$ . At each frequency, two plots are shown, the general shape of the cost functional, and its values at radii close to the optimum value.

It is observed that the quality of the approximation depends on the excitation fre-

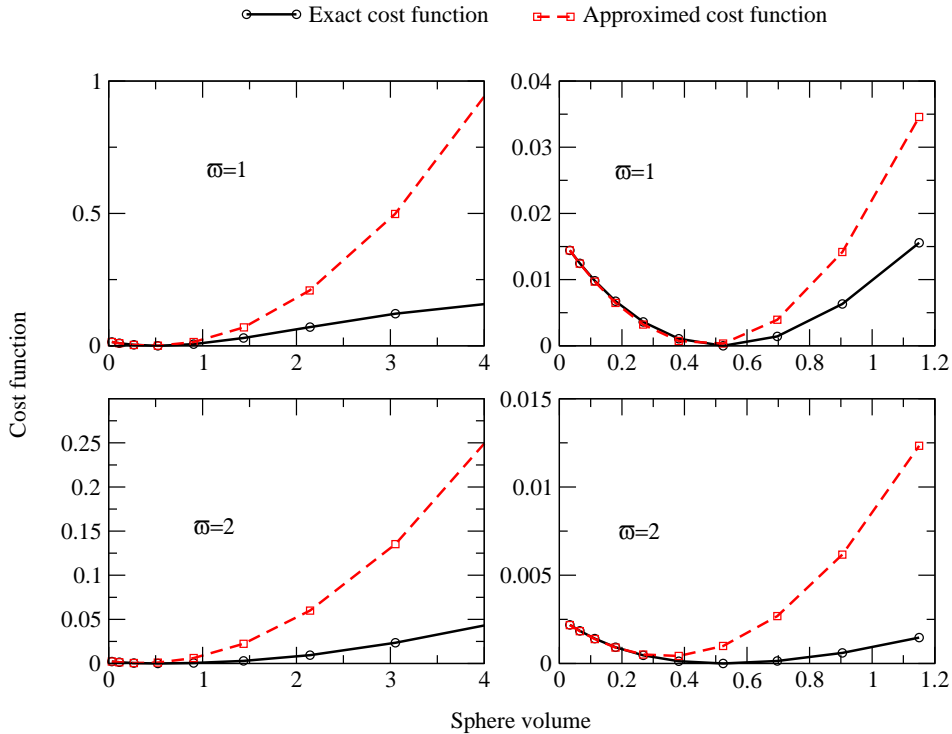


Figure 3: Comparison between the exact and the topological expansion cost functional for two frequencies.

quency. At frequency  $\bar{\omega} = 1.0$ , the optimum volume is quite the same, with error less than 1%. The optimum values at this frequency and point are  $\mathcal{V}^{\text{opt}} = 0.466r^3$  and  $a_r^{\text{opt}} = 0.481r$ . When the frequency is increased, the minimum value is reached at slightly different points,  $\mathcal{V}^{\text{opt}} = 0.394r^3$  and  $a_r^{\text{opt}} = 0.455r$ . The results are consistent with the TD approach since the approximation is better, the smaller is the cavity with respect to the dimensions of the problem. In this case, although the domain size is the same, the wave lengths are different. Recall that for  $\bar{\omega} = 1$ ,  $\lambda_s = 6.28r$ , while for  $\bar{\omega} = 2.0$ ,  $\lambda_s = 3.14$ . Plots also show that the approximation is good only for volumes close to the optimum one. The exact cost functional behaves different to the quadratic one for higher volume values.

Parameter	Value
Lower constrain	$[-2.5, -2.5, 0.5]$
Upper constrain	$[2.5, 2.5, 5.5]$
Number of parameters	3
Number of generations	50
Size of the population	20
Probability of crossover	0.8
Probability of mutation	0.02
Tournament probability	0.7
Scale for mutation	0.1

Table 1: Parameters of the GA for noise evaluation

### 7.1.3 Effect of noise in experimental data

Inverse problems are ill-conditioned. Convergence is not guaranteed, and results may not depend continuously on the data. In order to show the stability of the method, the dependence on errors in input data is checked in this section. To this end, noise is introduced in the pseudo-experimental values, through a random variable  $\varphi$  that pollutes these data,

$$u_i^{e,noise} = u_i^e (1 + \varphi) \quad (29)$$

Variable  $\varphi$  is uniformly distributed over the interval  $[-\eta, \eta]$ . Values of  $\eta$  tested in this study cover the range  $\eta = \{5\%, 10\%, 20\%\}$ . Again, four excitation frequencies have been considered,  $\bar{\omega} = \{1, 1.5, 2, 2.5\}$ .

The fitness function to maximize by the GA is simply  $f(\Gamma) = -\mathcal{J}(\Gamma)$ . In Tab. 1 the basic settings of the GA are shown. The three parameters are the cavity center coordinates  $(c_1, c_2, c_3)$ .

Fig. 4 and Fig. 5 show the results of the combined TD-GA at two tested frequencies. In Tab. 2 the parameter final values at each test, and the cost functional, are shown. The last column is the normalized error  $\frac{\varepsilon}{r}$  where,

$$\varepsilon = \sqrt{(c_1 - c_1^{\text{ref}})^2 + (c_2 - c_2^{\text{ref}})^2 + (c_3 - c_3^{\text{ref}})^2 + (a_r - a_r^{\text{ref}})^2} \quad (30)$$

with  $(c_1^{\text{ref}}, c_2^{\text{ref}}, c_3^{\text{ref}}, a_r^{\text{ref}}) = (0.0, 0.0, 3.0r, 0.5r)$ , the reference cavity parameters. In Fig. 6 the normalized error in terms of the excitation frequency and noise level is shown.

The optimization based on the GA is a stable algorithm, respect to noise in experimental measurements. Numerical tests confirm that noise levels up to 20%

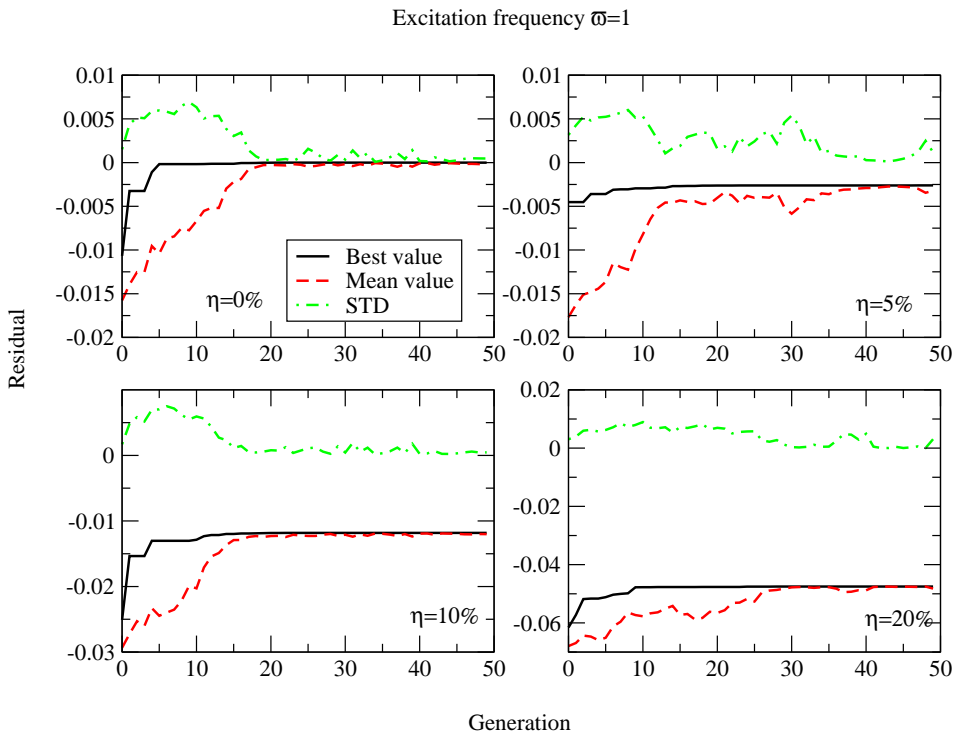


Figure 4: TD-GA identification of a cavity. Noise effect at  $\bar{\omega} = 1.0$

produces a solution close to the true cavity position. For each test, convergence is not guaranteed for noise levels up to 30%. This fact is related with the assumed errors that comes from the approximation of the cost functional. The higher the frequency, the higher the errors.

#### 7.1.4 Effect of material damping

Damping is included in the model through coefficients  $\xi_\alpha(\omega)$  and  $\xi_\beta(\omega)$ . This kind of damping is inherent to the material, and depends on the velocity of the particles. There is another kind of damping at the three-dimensional layer related with the radiation condition: the geometric damping. This mean that, in absence of material damping, the response to time-harmonic sources are progressive waves, and the resonance response can not occur.

Damping minimizes the effect of wave reflexions by surfaces. This fact leads to

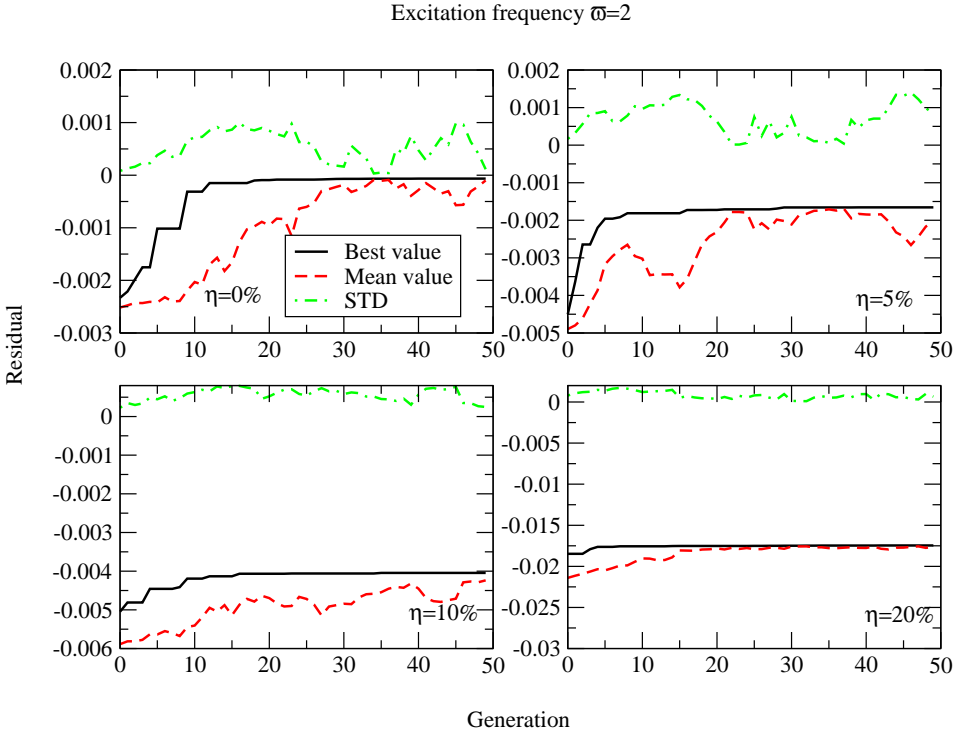


Figure 5: TD-GA identification of a cavity. Noise effect at  $\bar{\omega} = 2.0$

a better inversion, and this result is known in the literature. At this section, three damping rates have been considered;  $\xi_\alpha = \xi_\beta = \{2\%, 5\%, 10\%\}$ . In Tab. 3 the final values of the genetic algorithm search are shown. In all cases, the error decreases when damping increases. This fact is also observed in figures Fig. 7 and Fig. 8, in which the evolution of the computed parameters during the TD-GA search is plotted. Damping produces a faster and more stable identification: the Best Value curve require less iterations to obtain an stable value, the Standard Deviation diminishes faster and the Mean Value become more regular.

Material damping improves the convergence properties of any global search method, and in this case, it is also observed. The layer medium contains a natural radiation damping, even whith  $\xi_\alpha = \xi_\beta = 0\%$ . In absence of material damping it is more difficult to reach an final solution. For this the reason in the following sections, no material damping will be considered; in case of lack of convergence, a small damp- ing rate will be introduced, to observe the convergence properties. This procedure

Noise	$c_1/r$	$c_2/r$	$c_3/r$	$a_r/r$	$\tilde{\mathcal{J}}/(\mu r^3)$	$\varepsilon/r$
$\bar{\omega} = 1.0$						
0%	3.48E-04	5.39E-03	3.09	0.481	2.26E-06	9.02E-02
5%	-1.09E-01	2.49E-03	3.22	0.478	2.64E-03	2.47E-01
10%	1.52E-01	-1.24E-01	3.23	0.490	1.18E-02	3.09E-01
20%	-2.43E-02	2.46E-01	3.34	0.504	4.90E-02	4.20E-01
$\bar{\omega} = 1.5$						
0%	-1.98E-03	-1.39E-03	2.99	0.461	2.29E-01	4.03E-02
5%	4.48E-03	1.76E-01	2.88	0.464	1.30E-03	2.14E-01
10%	1.18E-02	-9.63E-02	2.91	0.485	4.19E-03	1.40E-01
20%	-2.77E-01	5.31E-02	2.73	0.469	2.39E-02	3.92E-01
$\bar{\omega} = 2.0$						
0%	5.06E-04	3.79E-03	3.15	0.455	6.54E-05	1.57E-01
5%	2.62E-02	-9.63E-02	3.20	0.485	1.65E-03	2.24E-01
10%	-2.04	1.73	5.11	0.703	4.04E-03	3.42
20%	2.07	1.82	1.94	0.393	1.74E-02	2.96
$\bar{\omega} = 2.5$						
0%	-7.44E-01	-4.44E-01	2.44	0.307	3.47E-04	1.12
5%	-3.43E-03	-7.78E-02	4.67	0.408	7.76E-04	1.67
10%	1.5	-1.92	4.43	0.523	2.60E-05	2.83
20%	-2.43	2.39	3.04	0.526	9.34E-03	3.41

Table 2: TD-GA global search. Final values of parameters. Random noise at measurements

is will prove critical in the context of multiple defect identification.

The particular way in which damping has been introduced, with  $\xi_\alpha = \xi_\beta$  involves that Poisson rate is real-valuated. In any case, the results are general enough. The aim of this section is only to check and conclude that, although radiation damping exists, material damping improves the convergence.

### 7.1.5 Combination of frequencies

At this section, the functional computed at four frequencies are combined. The new approximated cost functional is built by adding the contributions of each single frequency test. Thus, if  $\tilde{\mathcal{J}}(\bar{\omega}_i, \mathcal{V})$  denotes the approximated cost functional at

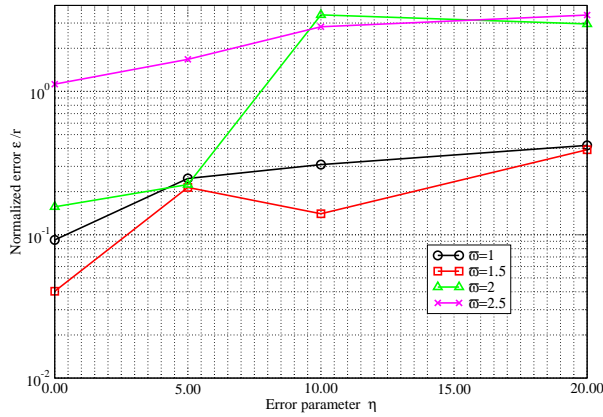


Figure 6: TD-GA global search. Effect of noise in measurements. Normalized errors. Dependence on the excitation frequency.

Damping (%)	$c_1/r$	$c_2/r$	$c_3/r$	$a_r/r$	$\mathcal{J}/(\mu r^3)$	$\epsilon/r$
$\bar{\omega} = 1$						
0	3.48E-04	5.39E-03	3.09	0.481	2.26E-06	9.02E-02
2	-2.98E-03	1.18E-03	3.09	0.484	1.54E-06	9.32E-02
5	-1.09E-02	2.13E-02	3.07	0.488	3.72E-06	7.46E-02
10	-2.91E-04	-6.22E-04	3.06	0.492	3.25E-07	6.12E-02
$\bar{\omega} = 2$						
0	5.06E-04	3.79E-03	3.15	0.455	6.54E-05	1.57E-01
2	-1.13E-03	-2.31E-03	3.12	0.456	2.24E-05	1.24E-01
5	-1.62E-03	3.87E-03	3.07	0.443	1.16E-05	8.71E-02
10	-1.44E-04	-4.21E-04	2.99	0.426	6.09E-06	7.53E-02

Table 3: TD-GA global search. Final values of parameters. Effect of material damping

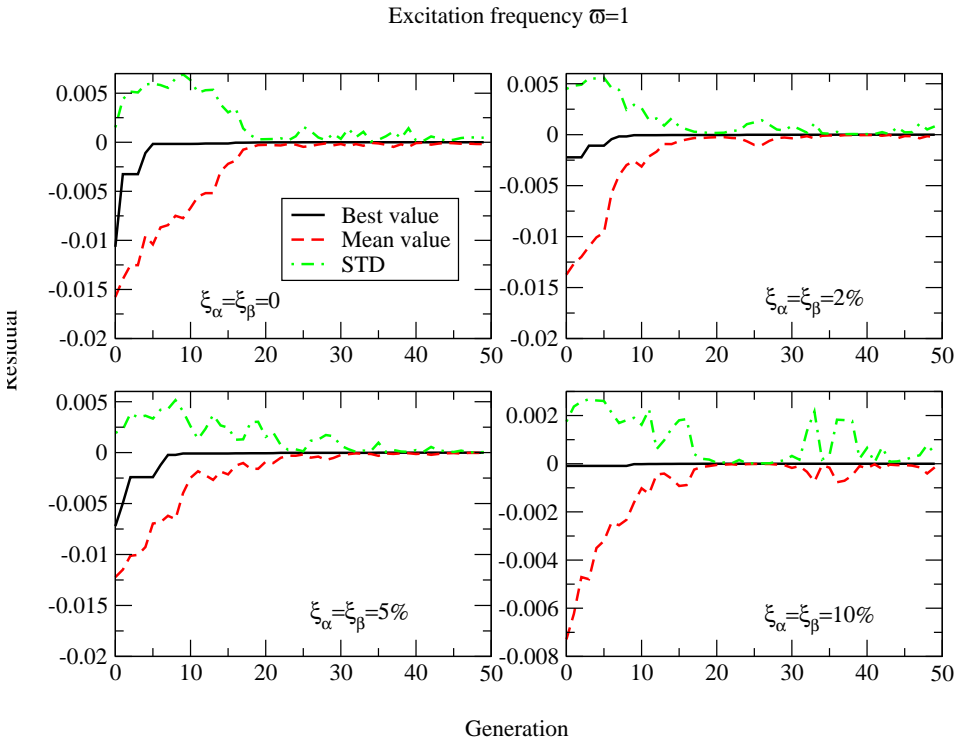


Figure 7: TD-GA identification of a cavity. Damping effect at  $\bar{\omega} = 1$

frequency  $\bar{\omega}_i$ , depending on  $\mathcal{V}$ , the combined approximated functional is built as,

$$\tilde{\mathcal{J}}(\mathcal{V}) = \sum_{i=1}^{NF} \tilde{\mathcal{J}}(\bar{\omega}_i, \mathcal{V}) \tag{31}$$

with  $NF$  the number of frequencies considered. Note that  $\mathcal{V}$  is a scalar value computed for the combined frequency cost functional.

In Tab. 4 the final parameters, cost functional, and normalized error computed with Eq. 30 are shown. The error with the combined cost functional is less than errors obtained at each individual frequency, but for  $\bar{\omega} = 1.5$ . This result means that for some individual frequencies, the result might be better, but providing more experiments is a stable approach to determine an optimum value.

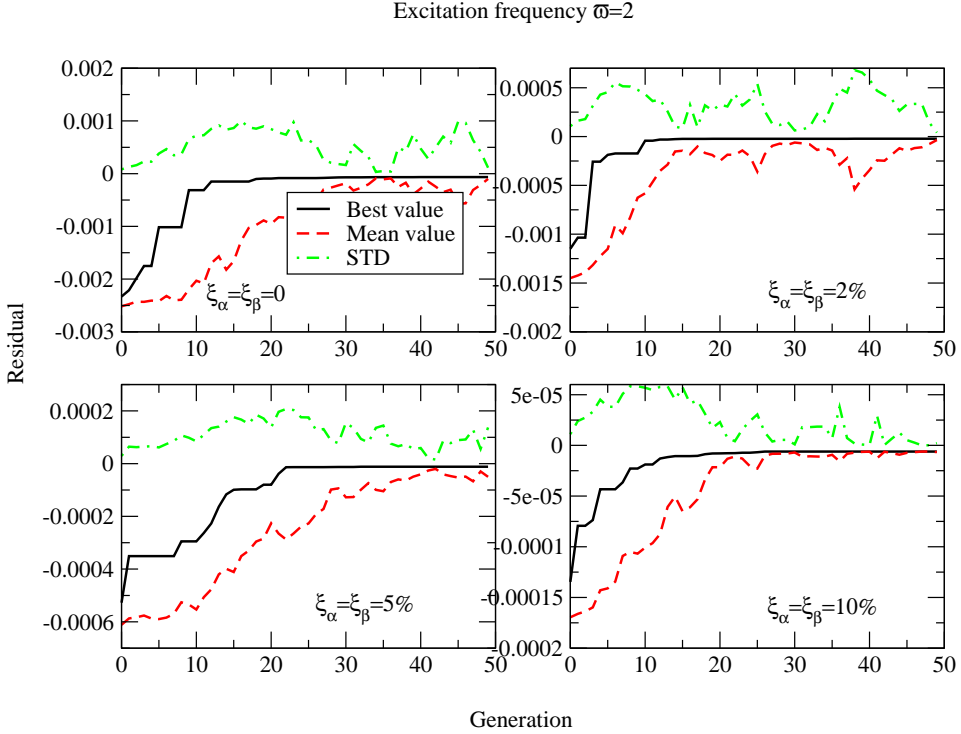


Figure 8: TD-GA identification of a cavity. Damping effect at  $\bar{\omega} = 2$

7.1.6 Effect of positions of sources/receivers

The identification of the hidden cavity with radius  $a_r = 0.5r$  centered at  $(0.0, 0.0, 3.0r)$  is carried out at this section with a non-symmetric profile of sources and receivers. The effect of multiple wave reflection is the main effect explored here. In Fig. 9 the position of the 16 sources (red) and 9 receivers (blue) is represented. Sources are centered at  $(-1.5r, 0.0, 0.0)$ , and located in a square patch of size  $2r \times 2r$ . Receivers are centered at  $(1.5r, 0.0, 0.0)$  and are disposed in a square patch of size  $2r \times 2r$ . The Boundary Element Mesh used to compute the pseudo-experimental data at the damaged state is shown as well in the figure.

The parameters shown Tab. 1 are used again for the combined TD-GA approach. The combination of frequencies is also explored. In Tab. 5 the final values, cost functional and error  $\varepsilon$  are shown. It is observed that although errors are the greatest for the lowest frequencies, when compared with the analogous test carried out for

$\bar{\omega}$	$c_1/r$	$c_2/r$	$c_3/r$	$a_r/r$	$\tilde{\mathcal{J}}/(\mu r^3)$	$\varepsilon/r$
1.0	3.48E-04	5.39E-03	3.09	0.4816	2.26E-06	9.20E-02
1.5	-1.98E-03	-1.39E-03	2.99	0.461	2.29E-01	4.03E-02
2.0	5.06E-04	3.79E-03	3.15	4.55E-01	6.54E-05	1.57E-01
2.5	-1.44E-01	-9.44E-01	2.44	3.08E-01	3.47E-04	1.12E+00
Combined	7.91E-03	4.66E-03	3.06	0.46246	2.28E-03	7.38E-02

Table 4: TD-GA global search. Combination of frequencies. Centered cavity with a symmetric profile of sources and receivers

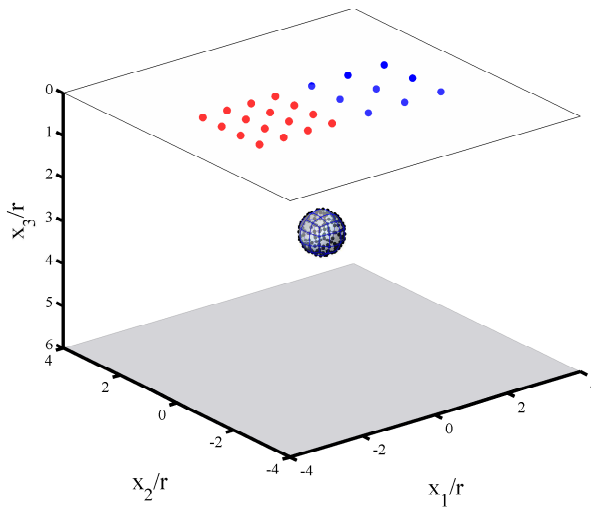


Figure 9: Configuration of sources (red) and receivers (blue). Identification of a centered cavity with a non-symmetric profile of sources and receivers

$\bar{\omega}$	$c_1/r$	$c_2/r$	$c_3/r$	$a_r/r$	$\tilde{\mathcal{J}}/(\mu r^3)$	$\varepsilon/r$
1.0	-3.24E-02	1.33E-03	3.153	0.488	3.08E-05	1.57E-01
1.5	1.58E-01	4.79E-03	3.040	0.489	6.35E-05	1.64E-01
2.0	8.59E-02	8.06E-03	3.028	0.437	4.71E-04	1.11E-01
2.5	2.37E-01	2.71E-03	3.039	0.427	2.27E-04	2.51E-01
Combined	6.92E-02	1.05E-03	3.059	0.463	1.73E-03	9.80E-02

Table 5: TD-GA global search. Spherical cavity identification. Non-symmetric profile of sources and receivers. Damping  $\xi = 0$ . Noise  $\eta = 0$ .

a symmetric profile of sources/receivers, in Tab. 4, lower errors are reported for higher frequencies.

The error of the combination of frequencies is less than the error obtained with any monochromatic test. In comparison with Tab. 4, the magnitude of the error obtained with the combination frequencies approach is similar. The inverse problem depends on the number of experiments. It is expected that the convergence is improved by increasing the number of experimental data.

### 7.2 Two cavities detection

The identification of two spherical cavities based on the linearization of the cost functional is explored in this section. It must be remarked that it is assumed that the interaction between cavities is null. Damping also minimizes the interaction between cavities. Thus, the sensitivity to damping is considered.

Since the aim is the identification of two cavities, the number of parameters for the GA search is 6, the coordinate centers of both cavities: for cavity  $\mathcal{C}_1$ , the center is  $(c_1^1, c_2^1, c_3^1)$  and its volume is  $\mathcal{V}_1$ . Cavity  $\mathcal{C}_2$  is centered at  $(c_1^2, c_2^2, c_3^2)$ , and has volume  $\mathcal{V}_2$ .

Given the cavity centers, a local expansion of the cost functional in terms of the two volumes is obtained. Optimum volumes are computed by solving a local constrained minimization problem as explained in section 6. Numerical tests confirm that the restrictions play an important role in order to obtain a convex approximated cost functional. This aspect is particularly important at the highest frequencies.

Parameters of the combined TD-GA global are shown in Tab. 6. Note that in this six-parameter identification, there are multiple minima, since the order of cavity 1 and 2 can be interchanged, leading to the same cost functional. Numerical tests confirm that multiple minima are obtained, but the global search is stable, in the sense that once the centers and volumes are fixed, the next generation preserves the

Parameter	Value
Low constrain	$[-2.5, -2.5, 0.5, -2.5, -2.5, 0.5]$
Up constrain	$[2.5, 2.5, 5.5, 2.5, 2.5, 5.5]$
Number of parameters	6
Number of generations	100
Size of the population	50
Probability of crossover	0.8
Probability of mutation	0.02
Tournament probability	0.7
Scale for mutation	0.1

Table 6: Parameters of the GA for two cavities identification

positions and sizes of the previous one.

### 7.2.1 Two cavities identification: Different diameters

For the first test cavities with different diameters are considered. Cavity  $\mathcal{C}_1$  is centered at  $(-1.5r, 0.0, 2.0r)$  and radius  $a_r^1 = 0.5r$ . The second cavity  $\mathcal{C}_2$  is located at  $(1.5r, 2.0r, 4.0r)$ , radius  $a_r^2 = 1.0r$ . In Fig. 10 the BE mesh used only to provide pseudo-experimental data by a forward solution at the damaged domain is shown; also, the location of sources and receivers are shown in the figure. The excitation frequency is fixed in  $\bar{\omega} = 1.0$ . Layer and material properties are like the ones considered for the other numerical tests.

The interaction between cavities worsens the approximated topological expansion of the cost functional. The interaction depends on damping, among other parameters (e.g. relative distance, excitation frequency, sources, receives, etc). Thus, better convergence results are expected when damping is included. In order to test it, damping rates  $\xi_\alpha = \xi_\beta = 5\%$  are considered in an independent test.

The combined TD-GA global search produces final values reported in Tab. 7. The last column represent the error computed for each cavity. Damping improves the convergence and minimizes the interaction between cavities, and leads to lower parameter errors  $\varepsilon$ .

### 7.2.2 Two cavities identification: Equal diameters

At the second test involving two cavities of equal size are considered. Cavity  $\mathcal{C}_1$  is centered at  $(1.0r, -1.0r, 4.0r)$  and radius  $a_r^1 = 0.5r$ . The second cavity  $\mathcal{C}_2$  is located at  $(-2.0r, 2.0r, 2.0r)$ , radius  $a_r^2 = 0.5r$ . In Fig. 11 the BE mesh and the location of

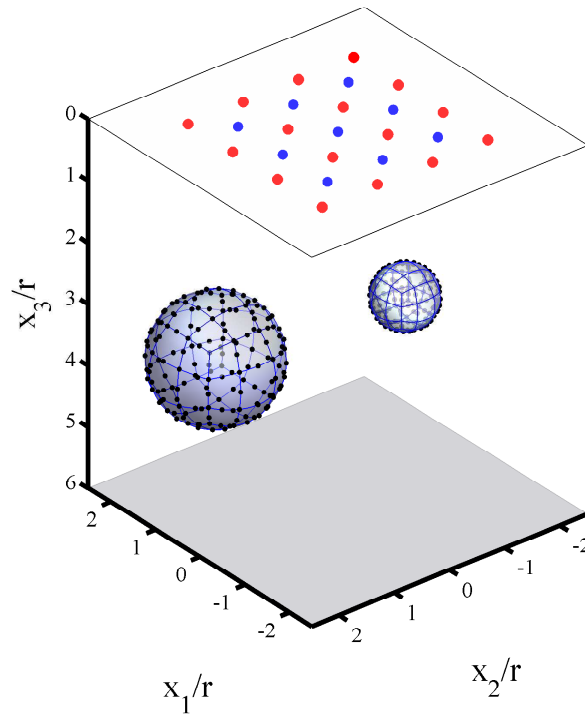


Figure 10: Two cavities identification. Different radius. Boundary elements mesh

Cavity	$c_1/r$	$c_2/r$	$c_3/r$	$a_r/r$	$\epsilon/r$
$\xi_\alpha = \xi_\beta = 0\%$					
$\mathcal{C}_1$	-1.80	0.12	2.07	0.48	0.33
$\mathcal{C}_2$	1.69	1.08	4.26	0.96	0.98
$\xi_\alpha = \xi_\beta = 5\%$					
$\mathcal{C}_1$	-1.48	0.15	2.11	0.47	0.19
$\mathcal{C}_2$	1.64	1.11	4.14	0.96	0.92

Table 7: TD-GA global search. Two cavities identification, different radius. Final values of parameters.

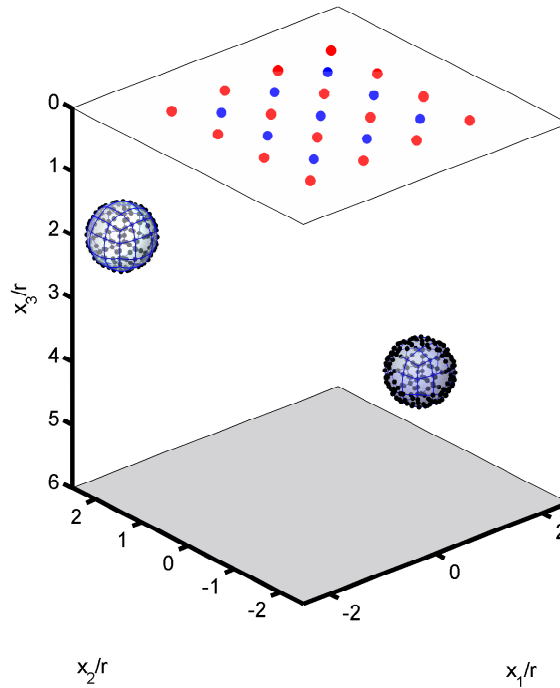


Figure 11: Two cavities identification. Same radius. Boundary Element mesh

sources and receivers are shown. The excitation frequency is also fixed at  $\bar{\omega} = 1.0$ , and the layer and material properties are like in previous tests.

The interaction between cavities is greater than the one for the previous test. Although the distances between cavities are similar, and the diameters are smaller, the position of sources and receivers leads to reflections of waves from one cavity to the other. In Tab. 8 the final results are shown, both when no damping is included and for a  $\xi_\alpha = \xi_\beta = 5\%$  damping level. When no damping is given, convergence is not attained. On the contrary, when damping is included, the error decreases strongly. Thus, material damping diminishes the effect of the interaction between cavities. This different behavior is also observed in Fig. 12, in which the residual strongly decays when damping is considered.

Cavity	$c_1/r$	$c_2/r$	$c_3/r$	$a_r/r$	$\varepsilon/r$
$\xi_\alpha = \xi_\beta = 0\%$					
$\mathcal{C}_1$	0.22	0.23	4.66	1.88	2.11
$\mathcal{C}_2$	-1.21	-1.22	2.31	1.19	3.40
$\xi_\alpha = \xi_\beta = 5\%$					
$\mathcal{C}_1$	1.00	-1.01	4.10	0.51	0.10
$\mathcal{C}_2$	-1.92	1.95	2.04	0.47	0.11

Table 8: TD-GA global search. Two cavities identification, same radius. Final values of parameters

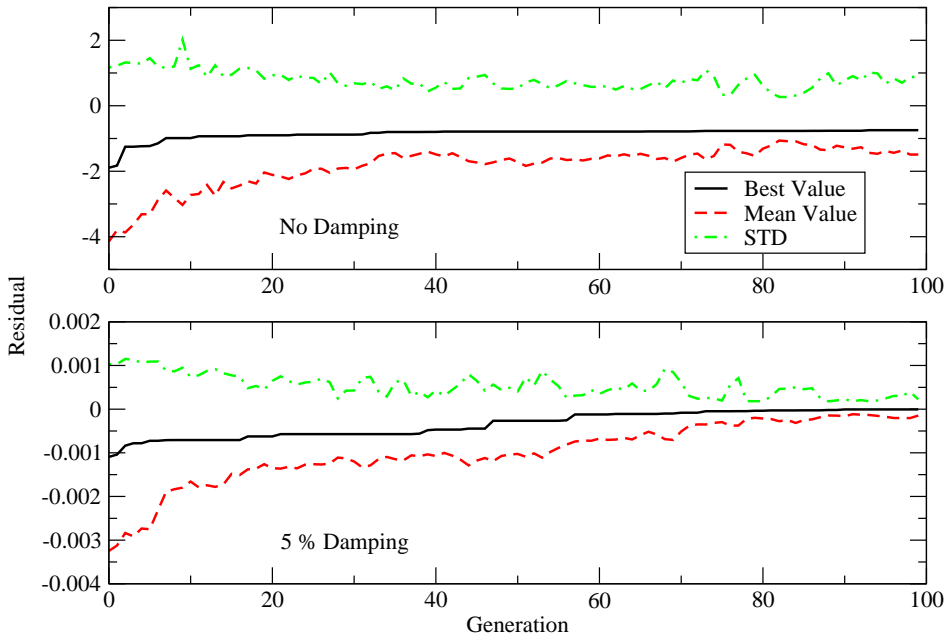


Figure 12: TD-GA identification of two cavities with the same diameters. Effect of damping at  $\bar{\omega} = 1$

### 7.3 Multiple defect identification without a-priori information on the number of cavities

One of the most interesting applications of the TD-GA approach is the possibility of inversion when the number of real cavities is smaller than the number of trial

Cavity	$c_1/r$	$c_2/r$	$c_3/r$	$a_r/r$
$\bar{\omega} = 1$				
$\mathcal{C}_1$	4.17E-01	3.36E-01	3.08	0.11
$\mathcal{C}_2$	-5.34E-03	-3.40E-03	3.09	0.48
$\bar{\omega} = 1.5$				
$\mathcal{C}_1$	8.04E-03	8.44E-02	4.22	0.18
$\mathcal{C}_2$	2.613E-03	-2.63E-03	2.99	0.46
$\bar{\omega} = 2$				
$\mathcal{C}_1$	-4.23E-01	8.13E-02	2.23	0.22
$\mathcal{C}_2$	-5.91E-02	3.24E-04	3.16	0.48
$\bar{\omega} = 2.5$				
$\mathcal{C}_1$	2.24E-02	-5.73E-02	3.08	0.36
$\mathcal{C}_2$	4.74E-02	-2.20E-01	5.29	0.36

Table 9: TD-GA global search. Identification of a single spherical cavity using two trial cavities.

cavities. The main advantage of the topological expansion is that zero volumes are obtained as natural solutions, in contrast with a forward solution based on the full DS. At each point, the local search is restricted to zero or positive radius, which has proved to be very important to define a cost functional with a strong local minimum.

At this section, the basic cavity identified in section 7.1 is considered. The true DS is a single cavity centered at  $(0.0, 0.0, 3.0r)$  with radius  $a_r = 0.5r$ . To solve the IIP a 6-parameter TD-GA is employed (two cavities). Parameters of the GA global search are those in Tab. 6. The symmetric profile of 16 sources and 9 receivers used in section 7.1 is employed here again.

In Tab. 9 the final results of the TD-GA global search is shown. It is observed that two cavities are obtained. One of them is close to the exact one. The second one has a small radius. This second small cavity depends on some parameters, such as damping, number of experiments, etc. The interaction between cavities is small when the frequency is low. This is the reason that, by increasing the frequency, a higher error is obtained. Actually, at the highest tested frequency,  $\bar{\omega} = 2.5$  it is observed that two equal-size cavities are obtained, with only one of them close to the true cavity. This test reveals that the consideration of the interaction between cavities becomes more important at the highest frequencies. As it was reported in tests involving two cavities, the global search can be improved by the consideration of an small material damping rate.

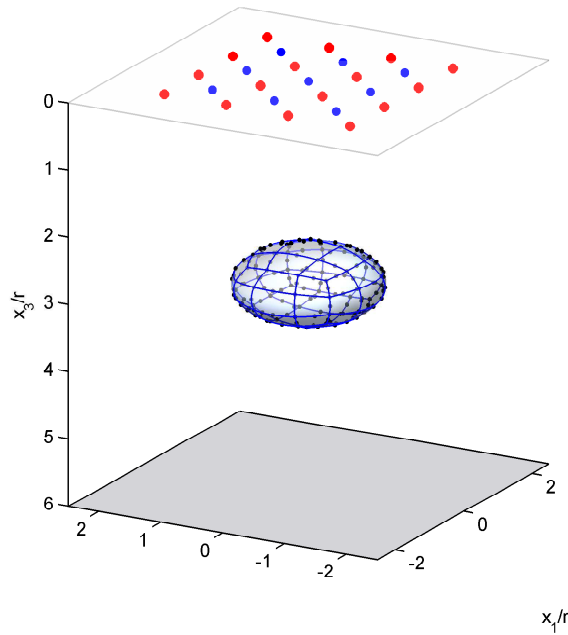


Figure 13: Oblate spheroid cavity. Boundary Element mesh

#### 7.4 Ellipsoidal cavity detection: oblate spheroid

At this section the identification of an oblate spheroid is tested, thus, the exact solution is not reachable. The algorithm is explored to check the potentiality of the method to provide a location and size of a cavity when the shape is not an sphere.

The ellipsoid has axes  $a = b = 2c = 1.1r$ , and it is centered at  $(0.0, 0.0, 3.0r)$ . The exact volume for the ellipsoid is  $\mathcal{V}^{\text{ref}} = 2.7876r^3$ . The symmetric profile of sources and receivers used at the identification of an spherical cavity is used. In Fig. 13 the BE mesh used to obtain the pseudo-experimental data, and the location of sources and receivers are shown.

For each frequency, the final results of the TD-GA approach are shown in Tab. 10. For each final-point, the quadratic error  $\varepsilon$  computed by

$$\varepsilon = \sqrt{(c_1 - c_1^{\text{ref}})^2 + (c_2 - c_2^{\text{ref}})^2 + (c_3 - c_3^{\text{ref}})^2 + (v - v^{\text{ref}})^2} \quad (32)$$

is presented, where non-dimensional parameters are employed here.

$\bar{\omega}$	$c_1/r$	$c_2/r$	$c_3/r$	$v/r^3$	$\mathcal{J}/(\mu r^3)$	$\varepsilon$
1	1.38E-03	1.06E-05	3.85	3.0297	8.04E-04	8.83E-01
1.5	-4.13E-04	1.74E-03	3.03	2.1752	1.23E-03	6.13E-01
2	1.66E-03	6.38E-03	3.25	1.2735	5.30E-03	1.53E+00
2.5	2.70E-03	-3.15E-02	2.59	1.1793	8.26E-03	1.66E+00

Table 10: TD-GA global search. Oblate ellipsoid. Final results and errors

## 8 Concluding Remarks

The topological expansion of the cost functional is presented for the layer domain in the context of time-harmonic problems. The small-asymptotic expansion of displacements in terms of a cavity volume is presented. The expansion is extended to the multi-defect case, neglecting the interaction between defects.

For a given location of a cavity center, the Cost Functional Expansion can be built and optimized in terms of volumes. This leads to the Optimal Cost Functional Expansion (OCFE). The volume optimization is carried out by a local constrained minimization since the volumes are non negative values. This aspect is very important in the context of frequency domain computations.

The search of the optimum position is then carried out by a global zero-order optimization algorithm (Genetic Algorithms). For a given set of cavity centers, the optimum volumes are computed and the OCFE is evaluated. This approach is particularly interesting for the multiple-defect global search. The proposed approximate cost functional allows the collapse of some cavities, providing a way to reduce the number of assumed cavities to fit the actual number of voids. This approach to find multiple cavities is sensitive to frequency and damping, due to the fact that the topological expansion worsen with decreasing wave-length, i.e. increasing frequency, and that the terms involving the interaction between cavities and surfaces are not included here. Such interactions decreases with increasing material damping and distances between cavities and surfaces.

The cost functional expansion depends on the shape of the defect. The problem involving spherical shapes has been considered here. Based on it, a test has been carried out in order to check the possibility of finding ellipsoids. Numerical test show that the center coordinates and the volumes are successfully found.

At the frequency domain, the information provided by different frequencies might be combined to generate a new cost functional. Numerical tests confirm that the results obtained by considering the combination of frequencies are usually better than the ones obtained for a monochromatic test.

**Acknowledgement:** The authors appreciate the financial support from the Spanish Ministry of Science and Innovation with Project DPI-2010-21590-C02, that funded the research discussed in this paper.

## References

- Bonnet, M.** (2009): Higher-order topological sensitivity for 2-D potential problems. application to fast identification of inclusions. *Int. J. Solids and Structures*, vol. 46, pp. 2275–2292.
- Bonnet, M.; Guzina, B. B.** (2004): Sounding of finite bodies by way of topological derivative. *International Journal for Numerical Methods in Engineering*, vol. 61, pp. 2344–2373.
- Christensen, R. M.** (1971): *Theory of viscoelasticity*. Academic Press, New York.
- Comino, L.; Gallego, R.; Rus, G.** (2008): Combining topological sensitivity and genetic algorithms for identification inverse problems in anisotropic materials. *Computational Mechanics*, vol. 41, pp. 231–242.
- Eschenauer, H. A.; Kobelev, V. V.; Schumacher, A.** (1994): Bubble method for topology and shape optimization of structures. *Structural Optimization*, vol. 8, pp. 42–51.
- Eshelby, J. D.** (1957): The determination of the elastic field of an ellipsoidal inclusion, and related problems. *Proceedings of the Royal Society of London. Series A. Mathematical and Physical Sciences*, vol. 241, no. 1226, pp. 376–396.
- Eshelby, J. D.** (1959): The elastic field outside an ellipsoidal inclusion. *Proceedings of the Royal Society of London. Series A. Mathematical and Physical Sciences*, vol. 252, no. 1271, pp. 561–569.
- Gallego, R.; Rus, G.** (2002): Identification of cracks and cavities using the topological sensitivity boundary integral equation. In *Proceedings of the IABEM 2002 Conference*, Austin, Texas.
- Gallego, R.; Rus, G.** (2004): Identification of cracks and cavities using the topological sensitivity boundary integral equation. *Computational Mechanics*, vol. 33, pp. 154–163.
- Guzina, B.; Chikichev, I.** (2007): From imaging to material identification: a generalized concept of topological sensitivity. *Journal of the Mechanics and Physics of Solids*, vol. 55, pp. 245–279.

**Guzina, B. B.; Bonnet, M.** (2004): Topological derivative for the inverse scattering of elastic waves. *Quarterly Journal of Mechanics and Applied Mathematics*, vol. 57, no. Part 2, pp. 161–179.

**Jackowska-Strumiłło, L.; Sokołowski, J.; Źochowski, A.** (1999): The topological derivative method and artificial neural networks for numerical solution of shape inverse problems. Rapport de Recherche 3739, Institute National de Recherche en Informatique et en Automatique, 1999.

**Lewiński, T.; Sokołowski, J.** (1997): Topological derivative for nucleation of non-circular voids. Rapport de Recherche 3798, Institute National de Recherche en Informatique et en Automatique, 1997.

**Lewiński, T.; Sokołowski, J.** (1998): Optimal shells formed on a sphere. the topological derivative method. Rapport de Recherche 3495, Institute National de Recherche en Informatique et en Automatique, 1998.

**Lewiński, T.; Sokołowski, J.** (2003): Energy change due to the appearance of cavities in elastic solids. *Int. J. Solids and Structures*, vol. 40, pp. 1765–1803.

**Martínez-Castro, A.; Gallego, R.** (2007): Three-dimensional Green's function for time-harmonic dynamics in a viscoelastic layer. *International Journal of Solids and Structures*, vol. 44, pp. 4541–4558.

**Schumacher, A.** (1995): *Topologieoptimierung von Bauteilstrukturen unter Verwendung von Lochpositionierungskriterien*. PhD thesis, University of Siegen, Germany, 1995.

**Sokołowski, J.; Źochowski, A.** (1997): On topological derivative in shape optimization. Rapport de Recherche 3170, Institute National de Recherche en Informatique et en Automatique, 1997.

**Sokołowski, J.; Źochowski, A.** (1998): Topological derivatives for elliptic equations. In *Proc. Inverse Problems, Control and Shape Optimization*, pp. 129—136.